Macromolecular Research

Article

DOI 10.1007/s13233-021-9075-7

www.springer.com/13233 pISSN 1598-5032 eISSN 2092-7673

Improved Pseudocapacitive Performance of Graphene Architectures Modulating by Nitrogen/Phosphorus Dual-Doping and Steam-Activation

Chaonan Wang[†,1]
Junhong Zhao[†,2]
Shengyun Luo[1]
Xu Yu[*,3]

[1] College of Materials Science and Engineering, Guizhou Minzu University, Guiyang, 550025, P. R. China
[2] School of Materials and Chemical Engineering, Zhengzhou University of Light Industry, Zhengzhou, 450002, P. R. China
[3] School of Chemistry and Chemical Engineering, Yangzhou University, Yangzhou, 225002, P. R. China

Received June 17, 2020 / Revised March 30, 2021 / Accepted July 22, 2021

Abstract: Steam-assistant nitrogen (N) and phosphorus (P) co-doping of graphene (s-NPG) architectures are constructed by a facile chemical converted method and thermal activation. Steam-activation treatment can provide abundant porous structure for fast ion diffusion and expose more electrochemical active-sites for surface faradic reaction. The wrinkled surface of S-NPG with a large surface area is probed by microscopic analysis. The spectroscopic analysis confirms the existence of pyridinic-N and C-P-O bonds for s-NPG, which are the dominant electroactive sites for accommodating the protons or charges. Therefore, s-NPG exhibits a high specific capacitance of 317 F g^{-1} at 1 A g^{-1} with a good rate capability of 87% and cyclic stability of 97.7% after 20,000 cycles. The excellent pseudocapacitive behavior can be attributed to the synergistic effect of hierarchical structure with and surface modification by N and P dual-doping. The simple steam-assistant treatment can be a potential way to construct the hierarchically structured electrode materials for supercapacitors.

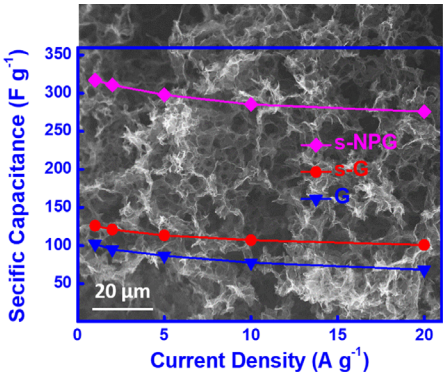

Keywords: steam activation, heteroatom, supercapacitor, architecture, graphene.

1. Introduction

Pseudocapacitors (PCs), as potential electrochemical capacitors, have attracted the attention to satisfy the fast growth of high-efficiency electrical applications due to the fast charge/discharge rate, high power density and long-term stability.[1-4] Meanwhile, the charge storage mechanism of PCs strongly depends on the surface redox reaction at or near the electrode/electrolyte interface, which is different from the diffusion-dominant intercalation or alloy/de-alloy mechanism of batteries. Graphene with the theoretic capacitance of ~550 F g^{-1} normally applies as the conductive substrate with high electrical conductivity and specific surface area.[5] However, the energy density is still one of the core challenges for the practical application of graphene-based nanomaterials, which can be improved by increasing the specific capacitance of electrode materials.[6-8]

The rational design of graphene-based nanomaterials by combining morphology and compositional optimization is an attractive strategy to improve the electrochemical behavior of supercapacitor devices.[9,10] The pseudocapacitive carbon and heteroatom doped graphene can show the significant enhancement of electrochemical performance as supercapacitors electrodes.[11,12] Many efforts have been devoted to constructing graphene hybrids with unique structures like one-dimensional (1D) nanofibers, two-dimensional porous film (2D) and three-dimensional (3D) architectures using electrospinning, vacuum-filtration and hydrothermal methods.[13-15] Especially, the high porosity of electrode materials was favorable to accelerate the electrolyte diffusion and improve the efficient utilization of the active sites near the surface; while the structural modulation of electrodes by cross-linking,[16,17] chemical activation[18,19] and physical activation[20,21] are important to improve the capacitive behaviors for practical applications. Ruoff's[18] and Guan's[22] groups demonstrate the preparation of porous carbon materials via chemical activation, which show the excellent electrochemical properties for supercapacitors. The nanomaterials produced by chemical activation should be well washed to remove the inorganic residues, which are still confronted with the problems like environmental pollution and the corrosion of the instruments. Differently, physical activation, as an effective method, could efficiently modulate the highly porous carbon materials with the different activation agents, as the reported work by Liu[23] and Han,[21] which can show the significant increase of the surface area.

Surface modification of graphene by heteroatoms doping can effectively tailor the electronic structures and surface properties.

Acknowledgments: This work is supported by the Projects of Science and Technology Department of Guizhou Province ([2017]1081, [2018]1085), and the Science and Technology Platform Talent Plan of Guizhou Province ([2018] 5773-YB13). Xu Yu also thanks the support of Natural Science Foundation of the Jiangsu Higher Education Institutions of China (18KJB150034). We also acknowledge the technical support at Testing Center of Yangzhou University.

***Corresponding Author:** Xu Yu (yxypz15@yzu.edu.cn)
[†]Chaonan Wang and Junhong Zhao contributed equally to this work.

Heteroatoms, like nitrogen (N), phosphorus (P), sulfur (S), and boron (B), possess different electronegativity and atomic radius from carbon atoms, which can dope into graphene lattices by forming covalent heteroatom-containing configurations as confirmed by the experimental and computational analysis.[24,25] The single or dual-doped graphene nanomaterials have been widely used in several applications, like lithium-ion batteries,[26,27] electrocatalysts for water splitting[28] and supercapacitors.[25,29,30] As reported by the lectures,[31-33] the N, S or P doped graphene aerogel can show excellent electrochemical performance due to the formation of pyridinic-N and P=O sites of C-P=O bonds as the dominant electroactive sites for fast faradic reaction. However, the N and P dual-doped graphene architecture with further steam-activation for high-performance supercapacitors has yet to be reported.

Herein, we successfully construct the steam-activated, N and P dual-doped graphene architecture (s-NPG) via the chemical converted method. Phytic acid and melamine as the heteroatom precursors dope into graphene lattices during the thermal steam-activation process. Especially, the steam-activation treatment can expand the layer distance and increase the porosity of s-NPG as probed by microscopic and spectra analysis. The formation of pyridinic N and C-P=O bond act as the dominant active-sites where the fast-redox reaction occurs, which is favorable to improve the pseudocapacitive behaviors. Due to the synergistic effect of highly porous structure and heteroatoms dual-doping, s-NPG exhibits excellent capacitive behaviors, like the high specific capacitance, good capacitance retention and cyclic stability.

2. Experimental

2.1. Preparation of s-NPG

The synthesis process of graphene aerogel is referred to the previous lecture.[7] First, 500 mg of iodine and 7.5 mL of hydrophosphoric acid were mixed as solution A. 200 mg of melamine, 0.6 mL of phytic acid and 5.5 mL of DI were mixed under bath-sonication as solution B. And then, 60 mg of graphene (5 mg mL^{-1}), solution A and solution B were mixed and sonicated for 30 min. The final mixture was placed in the oven at 80 ℃ for 10 h. The black hydrogel was washed by DI water until neutral and freeze-dried for 3 days. The aerogel was steam-activated at 900 ℃ for 1 h under an argon atmosphere and denoted as s-NPG. As a comparison, the steam-assistant graphene aerogel without heteroatoms doping was prepared with the same method and denoted as s-GA. The graphene aerogel without heteroatom doping and steam-treatment was also prepared with the same method and denoted as GA.

2.2. Characterization

Powder X-ray diffraction (XRD) patterns were conducted on empyrean (PAN analytical B.V., Holland) using Cu Ka radiation (λ = 1.54056 Å) radiation source operating at 40 kV and 40 mA at a scanning rate of 5° min^{-1}. The morphology and microstructure of the product were examined by field-emission scanning electron microscopy (FESEM) on an S-4800 II (Hitachi, Japan) and transmission electron microscopy (TEM) on TECNAI 12 (Philips, Holland), respectively. High-resolution transmission electron microscopy (HRTEM) was performed on an FEI Tecnai G2 F30 STWIN (USA) operating at 300 kV. Surface analysis of the sample was recorded by X-ray photoelectron spectroscopy (XPS) on ESCA LAB 250Xi (Thermo Science, USA). Raman spectra were carried out on a JobinYvon Micro-Raman Spectroscopy on RamLab-010, equipped with a holographic grating of 1800 lines mm^{-1} and a He-Ne laser (532 nm) as the excitation source. The specific surface area of the sample was tested by N_2 adsorption/desorption isotherms on a Brunauere Emmette Teller apparatus (BET, BELSORP-miniII) and BarretteJoynereHalenda (BJH) model was induced to calculate the pore size distributions.

2.3. Electrochemical measurements

The electrochemical performance of all prepared nanomaterials was measured by cyclic voltammetry (CV), galvanostatic charge/discharge (GCD) and electrochemical impedance spectroscopy (EIS) using a three-electrode configuration in a 1 M H_2SO_4 aqueous solution. The electrode material acted as the working electrode, Pt wire as the counter electrode and Ag/AgCl as the reference electrode. The detailed process for the preparation of the electrode materials was illustrated below. The aerogel was cut into a small rectangular slice with a size of 0.2 cm × 0.2 cm and attached on a stainless substrate by silver paste. And then, the electrode was placed in a vacuum oven at 60 ℃ for overnight. Finally, the electrode was ready for the working electrode. Cyclic voltammetry was measured at various scan rate from 10 to 200 mV s^{-1} with the potential window of 1.0 V; while GCD was measured at different current densities from 1 to 20 A g^{-1} with the potential window of 1.0 V. The electrochemical impedance spectroscopy was checked with the frequency range from 10^{-3} to 10^{6} Hz at the amplitude potential of 5 mV.

The specific capacitance was calculated by the integration area of CV curves as the following equation: $C = \int IdV(\Delta V \times m \times v)$. Where V is the applied voltage (V), I is current (A), v is scan rate (V/s) and m is the mass of the single electrode material (g). And the specific capacitance was calculated from GCD curves following the listed equation: $C = I/M(dV/dt)$, where I is the applied current, m is the mass of electrode, t is discharge time after IR drop, V is the applied voltage potential, respectively.

3. Results and discussion

3.1. The fabrication of s-NPG

The heteroatoms nitrogen (N) and phosphorus (P) dual-doped graphene architecture were constructed by chemical converted method and steam-activation, as illustrated in Figure 1. To construct the hierarchical architecture, the homogeneous property of the final mixture was crucial to be prepared through bath-sonication and magnetic stirring. And the final solution was placed in an oven at 80 ℃ for 10 h to form the melamine and phytic acid-functionalized graphene hydrogel by the cross-linked graphene nanosheets and the formation of hydrogen bonding. Subsequently, the surface-functionalized hydrogel was converted to

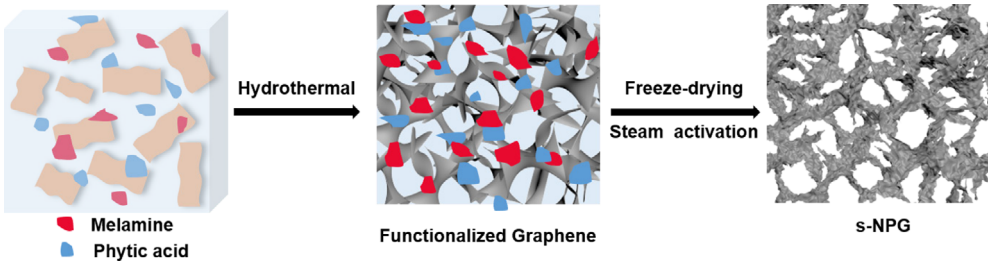

Figure 1. The schematic synthesis of s-NPG.

the aerogel through the ice-frozen and freeze-drying treatment. Finally, the heteroatoms N and P dual doped graphene aerogel was obtained by further steam-activation treatment at 900 ℃.

3.2. The morphology and structure of s-NPG

To characterize the surface morphology of s-NPG, scanning electron microscopy (SEM) was initially probed in Figure 2(a) and 2(b). s-NPG shows the well-maintained hierarchical structure, and the roughness of s-NPG is increased attributing to the incorporation of heteroatoms N and P. The porosity of s-NPG was evaluated by nitrogen adsorption/desorption isotherms (Figure 2(c) and Table 1). The specific surface area of s-NPG (456 $m^2 g^{-1}$) is larger than that of s-GA (374 $m^2 g^{-1}$) and GA (325 $m^2 g^{-1}$); while s-NPG exhibits the average mesopore diameter of 7.9 nm. s-GA exhibits a larger surface area than GA due to the expanded layer distance by steam-activation treatment; while the surface area for s-NPG is larger than that of s-GA owing to the further heteroatoms doping. As the transition electron microscopy (TEM) images are shown in Figure 2(d), s-NPG exhibits a crumpled surface due to the heteroatoms N and P dual-doping. The formation of nitrogen- and phosphorus-containing functional groups in the graphene matrix can distort the lattice structure of graphene by the different electronegativity and atomic radius of heteroatoms from carbon atoms. The energy-dispersive X-ray (EDX) spectra demonstrate that the corresponded elements are uniformly distributed on the graphene matrix,

Table 1. The surface area, pore volume, and mesopore size of s-NPG, s-GA, and GA

Sample	Surface area ($m^2 g^{-1}$)	Pore volume ($cm^3 g^{-1}$)	Mesopore size (nm)
s-NPG	456	92.6	7.9
s-GA	374	78.5	9.6
GA	325	72.9	10.5

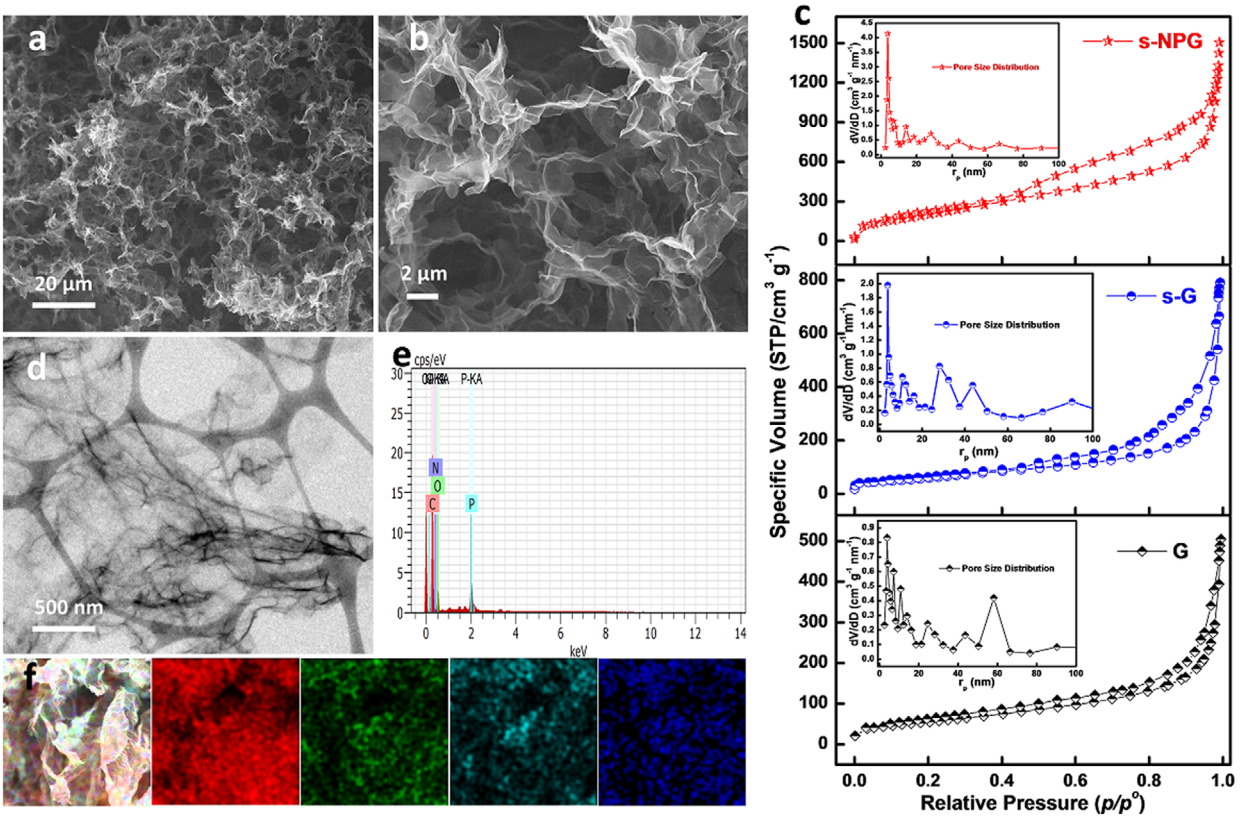

Figure 2. (a,b) SEM images of s-NPG. (c) Nitrogen adsorption/desorption isotherms of GA, s-GA, and s-NPG. (d) TEM image of s-NPG. (e) Energy dispersive X-ray analysis of s-NPG. (f) Elemental mapping images of s-NPG.

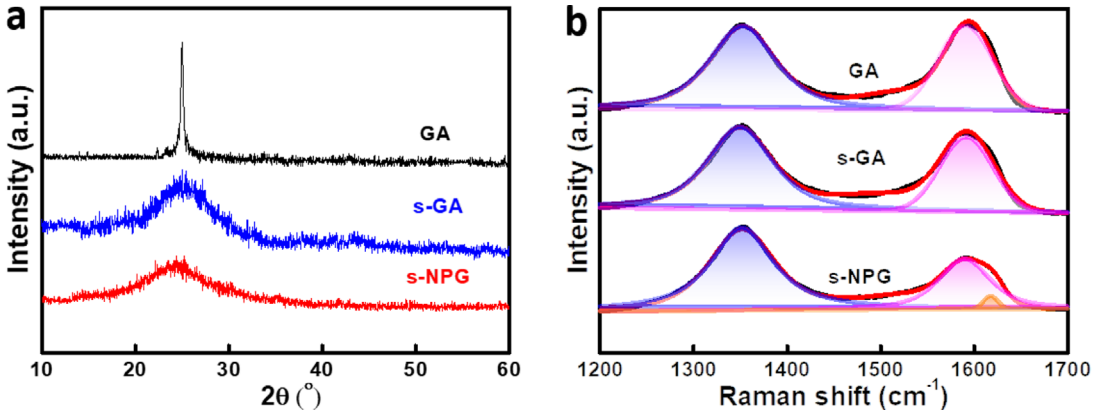

Figure 3. (a) XRD and (b) Raman spectra of GA, s-GA, and s-NPG.

implying the successful heteroatoms N and P doping (Figure 2(e) and 2(f)).

The structure and crystallinity of s-NPG were confirmed by X-ray diffraction (XRD) and Raman spectra (Figure 3). One clear peak appeared at 2θ =15° corresponding to the (002) plane of graphene oxide.[34] After the chemical conversion treatment, GA shows one strong (002) peak at 2θ =24.4° implying the reduction of graphene oxide (Figure 3(a)). In contrast to GA, s-GA exhibited a weak peak at 2θ =25.2° indicating a decrease of crystallinity by additional steam-activation treatment, while the (002) peak intensity for s-NPG was more weaken and broaden than that of s-GA attributing to the distorted structure of graphene matrix by heteroatom doping. During the thermal activation, the heteroatoms are incorporated into the graphene matrix following the decomposition of related precursors. The crystalline nature and surface environment of s-NPG were further confirmed by Raman spectra (Figure 3(b)). GA exhibits two typical peaks at 1351 cm^{-1} of the D band and 1592 cm^{-1} of the G band, respectively. While the D band and G band for s-NPG both show a slight down-shift in contrast to GA and s-GA, which can be attributed to the distortion of the graphitic structure. It is well known that the I_D/I_G ratio is an important factor to evaluate the formation of vacancies or defects.[31] The I_D/I_G value of s-NPG (1.16) is larger than that of s-GA (1.10) and GA (1.02), and the appearance of one shoulder peak of G band at 1617 cm^{-1}, implying a low graphitic degree of s-NPG due to the generation of defects by heteroatoms doping, which is consistent with the XRD analysis. As probed by XRD and Raman, s-NPG can be predicted to show good electrochemical performance, because the degradation of crystallinity and distorted graphitic structure is helpful to accelerate the electrolyte diffusion, expose more active sites and improve the utilization of effective sites.

3.3. The chemical states of s-NPG surface

To evaluate the change of surface chemistry and bonding configurations for s-NPG, X-ray photoelectron spectroscopy (XPS) was carried out in Figure 4. Figure 4(a) shows the full scan XPS spectra of s-NPG with four peaks at 133, 284, 400, and 531 eV, which correspond to P 2p, C 1s, N 1s, and O 1s with the atomic percent of 3.9%, 89.2%, 2.4%, and 4.5%, respectively. As deconvoluted by high-resolution C 1s spectra (Figure 4(b)), four peaks at 288.7, 285.4, 284.8, and 284.4 eV correspond to C=O, C-N, C-P, and C-C, respectively. The formation of C-N and C-P bonds strongly demonstrates the successful heteroatoms N and P dual-doping into graphene matrix. Furthermore, the N 1s spectra can be fitted into four peaks (Figure 4(c)). The two peaks centering at 397.0 and 398.1 eV correspond to the formation of pyridinic- and pyrrolic-N, and the peaks located at 400.2 and 402.7 eV are assigned to be graphitic nitrogen and oxidized nitrogen, respectively. The P 2p peak can be divided into C-P and P=O bonds at 132.9 and 133.8 eV (Figure 4(d)). Especially, the pyridinic nitrogen and P=O sites of the C-P=O bond had been demonstrated as the dominant active sites to improve the capacitive behavior of the electrode. By combining the hierarchical structure and surface chemistry change, it can be predicted that s-NPG can show a good electrochemical performance.

3.4. The capacitive behavior of s-NPG

To initially investigate the electro-capacitive behaviors of s-NPG, the CV and GCD were probed by a three-electrode configuration in a 1M H_2SO_4 aqueous solution with an applied voltage window of 1.0 V (Figure 5). s-NPG exhibits a nearly rectangular shape at the scan rate of 10 mV s^{-1}, which is similar to s-GA and GA implying the excellent ion diffusion at the electrode/electrolyte interface as the electrical double layer capacitance mechanism. The specific current density of s-NPG is larger than that of s-GA and GA. While the specific capacitance of s-NPG was calculated to be 307 F g^{-1} by integrating the CV curves, which was 1.5 and 2.1 times higher than that of s-GA and GA (Figure 5(a)). This result can be ascribed to the formation of pseudocapacitance after heteroatom doping. Furthermore, the pseudocapacitive behavior of s-NPG was confirmed by GCD with various current densities from 1 A g^{-1} to 20 A g^{-1}. As shown in Figure 5(b), s-NPG exhibited a smaller IR drop in the discharge curve than s-GA and GA, implying the low interior resistance and high electrical conductivity of s-NPG. While the asymmetric charge/discharge curves for s-NPG can be ascribed to the combination of electrical double-layer capacitance and fast reversible pseudocapacitance. To further confirm the steam-assistant activation and heteroatoms doping effects for the improvement of electrochemical performance, the specific capacitance was calculated from the GCD discharge curve (Figure 5(c)). The specific capacitance of

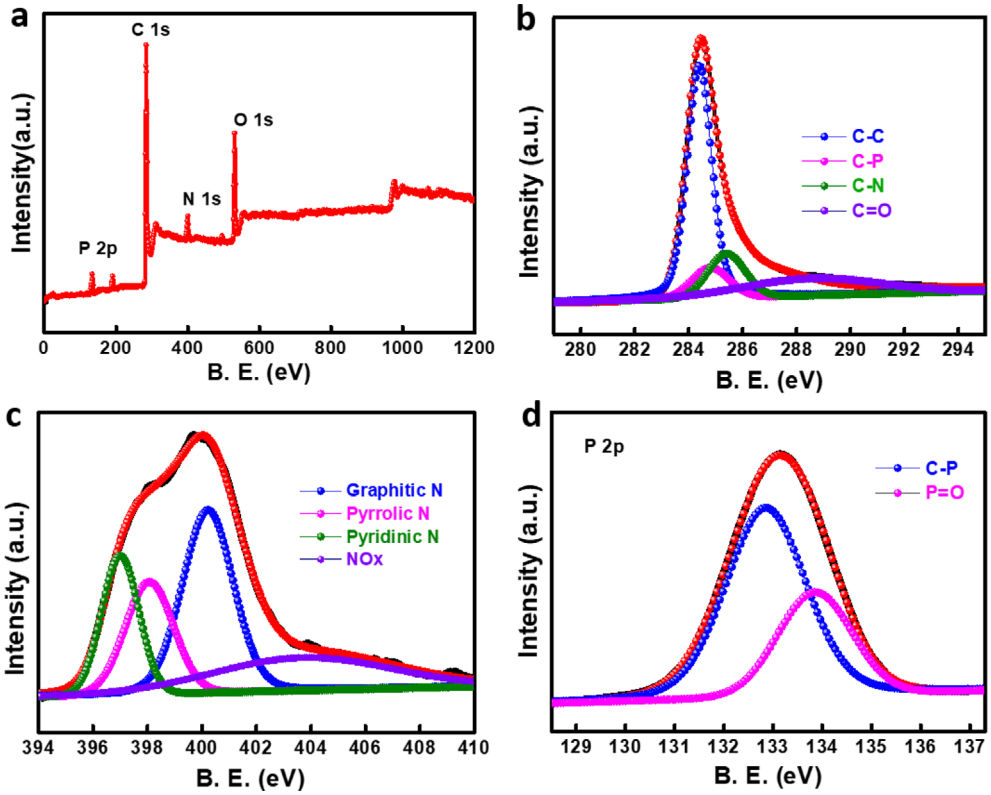

Figure 4. (a) Full XPS scan of s-NPG. High-resolution of (b) C 1s, (c) N 1s, and (d) P 2p spectra for s-NPG.

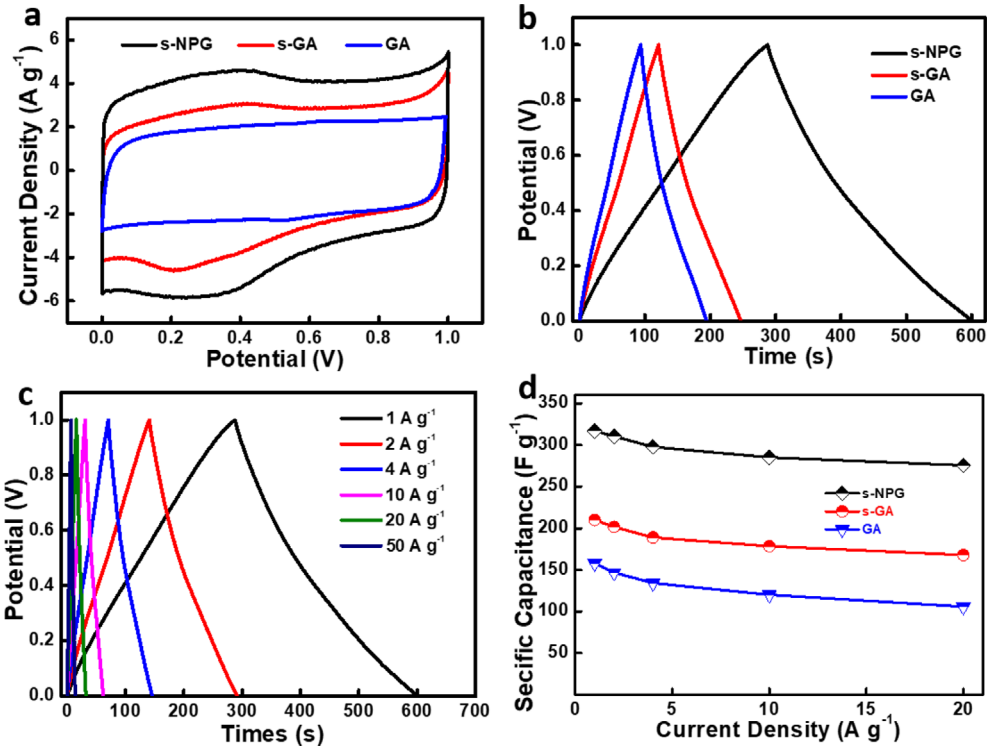

Figure 5. (a) CV curves of GA, s-GA and s-NPG at the scan rate of 10 mV s^{-1}. (b) GCD curves of GA, s-GA, and s-NPG at the current density of 1 A g^{-1}. (c) GCD curves of s-NPG at various current densities. (d) The rate capability of GA, s-GA, and s-NPG.

s-GA was an approach to 210 F g^{-1}, which is 52 F g^{-1} higher than that of GA. As the current density increased to be 20 A g^{-1}, s-GA showed only 42 F g^{-1} of capacitance loss with better capacitance retention of 80% than GA (67%) (Figure 5(d)). This result demonstrated that the electrochemical behavior for electrode materials can be improved by steam-activation treatment, which can expand the layer distance to expose more effective electro-active sites. Meanwhile, the specific capacitance of s-

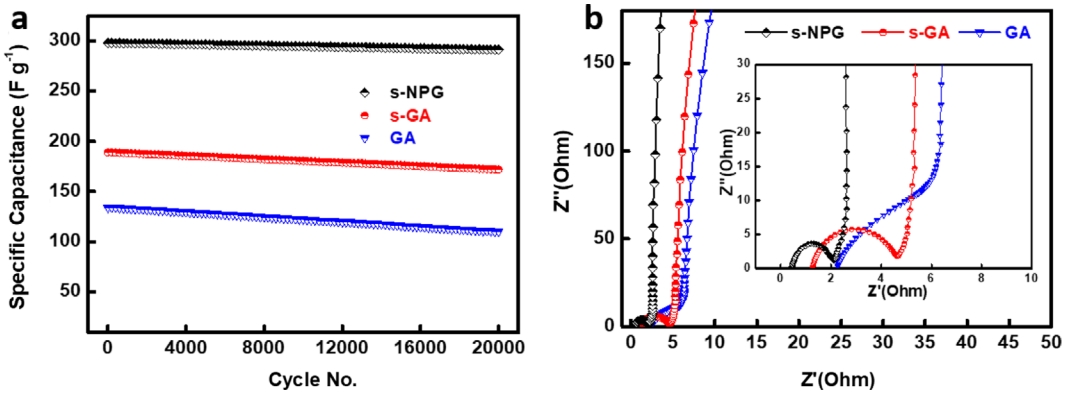

Figure 6. (a) Cyclic stability of GA, s-GA, and s-NPG. (b) Nyquist plot of GA, s-GA, and s-NPG (inset: the magnified Nyquist plot of GA, s-GA, and s-NPG).

NPG was 317 F g^{-1} with the capacitance retention of 87%, which was significantly increased in contrast to s-GA due to the heteroatoms doping. Especially, s-NPG can retain the capacitance retention of 78% at the current density of 50 A g^{-1}. This result demonstrated that the improvement of electrochemical behavior for s-NPG was attributed to the uniform heteroatoms doping with the formation of heteroatoms-containing functional groups as electro-active sites. The high specific capacitance and good rate capability for s-NPG can be ascribed to the formation of electro-active sites, which are favorable to accommodate lots of proton or electron on the surface of graphene nanosheet for fast redox reaction.

Long-life cyclic stability was an important factor to evaluate the electrochemical behavior of electrode materials for supercapacitors. The cyclic stability of s-NPG was measured continuous GCD measurement for 20000 cycles at the current density of 4 A g^{-1} (Figure 6(a)). In contrast to the initial cycle, the specific capacitance of s-NPG at the 20000th cycle is decreased from 298 F g^{-1} to 291 F g^{-1} with the capacitance retention of 97.7%, which is higher than that of s-GA (91%) and GA (82%) indicating excellent cyclic stability for s-NPG. To explore the ion-diffusion kinetics during the redox reaction process, electrochemical impedance spectroscopy was probed with a frequency from 10^{-3} to 10^{6} Hz (Figure 6(b)). It can be observed that s-NPG exhibits a small interior resistance comparison with s-GA and GA in the high-frequency region. In the high-mid region, the diameter of the semi-circle represented the charge transfer (R_{ct}) resistance during the charge/discharge process. S-NPG exhibits a smaller value of 2.05 Ω than that of s-GA and GA indicating a high electrical conductivity for fast charge migration. These excellent pseudocapacitive behaviors of s-NPG can be assigned from the synergistic effect of hierarchical structure and the surface composition change by heteroatoms doping.

As demonstrated by the abovementioned evidence, s-NPG with the hierarchical architecture can show an excellent pseudocapacitive behavior due to the synergistic effect of unique structural morphology and surface modification of the graphene matrix. The unique structure was assigned from the self-assembly and heteroatoms incorporation of graphene matrix following the steam-activation treatment, which can further explore more efficient electro-active sites. While the hierarchical can also provide fast ion diffusion pathways and accommodate a lot of charges during the charge/discharge process. Furthermore, the formation of N- and P-containing functional groups acted as the electro-active sites whereas fast faradic reaction occurred. The increased utilization of electro-active sites was favorable to improve the electrochemical performance with the generation of additional 'pseudocapacitance' during the charge/discharge process .

4. Conclusions

Herein, the steam-assistant heteroatoms N and P dual-doped graphene aerogel (s-NPG) was constructed by a facile chemical converted method and thermal activation approach. Herein, the melamine was used nitrogen precursor and phytic acid as phosphorus precursor sources. s-NPG electrodes exhibited a huge large specific surface area with the wrinkled feature to expose abundant electrochemical active sites. By the synergistic effect of the steam-activation and co-doping, s-NPG showed improved capacitive performance such as high specific capacitance of 317 F g^{-1} at 1 A g^{-1}, good rate capability of 87% and excellent capacitance retention of 97.7% over 20,000 charges/discharge cycles at 4 A g^{-1}. These results indicated that the hierarchically structured s-NPG can be a promising pseudocapacitive electrode for high-performance supercapacitors.

References

(1) R. Chen, M. Yu, R. P. Sahu, I. K. Puri, and I. Zhitomirsky, *Adv. Energy Mater.*, **10**, 1903848 (2020).
(2) L. Ma, J. Liu, S. Lv, Q. Zhou, X. Shen, S. Mo, and H. Tong, *J. Mater. Chem. A*, **7**, 7591 (2019).
(3) Q. Mahmood, S. K. Park, K. D. Kwon, S.-J. Chang, J.-Y. Hong, G. Shen, Y. M. Jung, T. J. Park, S. W. Khang, W. S. Kim, J. Kong, and H. S. Park, *Adv. Energy Mater.*, **6**, 1501115 (2015).
(4) P. Nakhanivej, X. Yu, S. K. Park, S. Kim, J.-Y. Hong, H. J. Kim, W. Lee, J. Y. Hwang, J. E. Yang, C. Wolverton, J. Kong, M. Chhowalla, and H. S. Park, *Nat. Mater.*, **18**, 156 (2019).
(5) J. Xia, F. Chen, J. Li, and N. Tao, *Nat. Nanotechnol.*, **4**, 505 (2009).
(6) Q. Yang, Z. Xu, B. Fang, T. Huang, S. Cai, H. Chen, Y. Liu, K. Gopalsamy, W. Gao, and C. Gao, *J. Mater. Chem. A*, **5**, 22113 (2017).
(7) X. Yu, Y. Kang, and H. S. Park, *Carbon*, **101**, 49 (2016).
(8) K. Fujisawa, R. Cruz-Silva, K. S. Yang, Y. A. Kim, T. Hayashi, M. Endo, M. Terrones, and M. S. Dresselhaus, *J. Mater. Chem. A*, **2**, 9532 (2014).

(9) G. Lee and J. Jang, *J. Power Sources*, **423**, 115 (2019).
(10) L. Liu, Y. Yan, Z. Cai, S. Lin, and X. Hu, *Adv. Mater. Interfaces*, **5** (2018).
(11) X. Yu, S. Yun, J. S. Yeon, P. Bhattacharya, L. Wang, S. W. Lee, X. Hu, and H. S. Park, *Adv. Energy Mater.*, **8**, 1702930 (2018).
(12) J.-Y. Hong, E.-H. Sohn, S. Park, and H. S. Park, *Chem. Eng. J,*. **269**, 229 (2015).
(13) J. H. Park, H. H. Rana, J. Y. Lee, and H. S. Park, *J. Mater. Chem. A*, **7**, 16962 (2019).
(14) Z. Zhou, W. Panatdasirisuk, T. S. Mathis, B. Anasori, C. Lu, X. Zhang, Z. Liao, Y. Gogotsi, and S. Yang, *Nanoscale*, **10**, 6005 (2018).
(15) X. Yu, M. Kota, and H. S. Park, *Macromol. Res.*, **25**, 1043 (2017).
(16) Y. Yuan, H. Lv, Q. Xu, H. Liu, and Y. Wang, *Nanoscale*, **11**, 4318 (2019).
(17) Z. U. Khan, T. Yan, L. Shi, and D. Zhang, *Environ. Sci.: Nano*, **5**, 980 (2018).
(18) Y. Zhu, S. Murali, M. D. Stoller, K. J. Ganesh, W. Cai, P. J. Ferreira, A. Pirkle, R. M. Wallace, K. A. Cychosz, M. Thommes, D. Su, E. A. Stach, and R. S. Ruoff, *Science*, **332**, 1537 (2011).
(19) L. Zhang, F. Zhang, X. Yang, G. Long, Y. Wu, T. Zhang, K. Leng, Y. Huang, Y. Ma, A. Yu, and Y. Chen, *Sci. Rep.*, **3**, 1408 (2013).
(20) J. Górka and M. Jaroniec, *Carbon*, **49**, 154 (2011).
(21) Z. Sui, Q. Meng, J. Li, J. Zhu, Y. Cui, and B. Han, *J. Mater. Chem. A*, **2**, 9891 (2014).
(22) M. Zhou, F. Pu, Z. Wang, and S. Guan, *Carbon*, **68**, 185 (2014).
(23) S. Liu, W. Peng, H. Sun, and S. Wang, *Nanoscale*, **6**, 766 (2014).
(24) S. Boukhalfa, D. Gordon, L. He, Y. B. Melnichenko, N. Nitta, A. Magasinski, and G. Yushin, *ACS Nano*, **8**, 2495 (2014).
(25) J. P. Paraknowitsch and A. Thomas, *Energy Environ. Sci.*, **6**, 2839 (2013).
(26) M. Yang, Y. Zhong, J. Bao, X. Zhou, J. Wei, and Z. Zhou, *J. Mater. Chem. A*, **3**, 11387 (2015).
(27) Y. Kang, X. Yu, M. Kota, and H. S. Park, *J. Alloys Compd.*, **726**, 88 (2017).
(28) L. Chen, J. Chang, Y. Zhang, Z. Gao, D. Wu, F. Xu, Y. Guo, and K. Jiang, *Chem. Commun.*, **55**, 3406 (2019).
(29) W. Chen, Z. Zhao, and X. Yu, *Electrochim. Acta*, **341**, 136044 (2020).
(30) Y. S. Yun, S. Y. Cho, and H.-J. Jin, *Macromol. Res.*, **22**, 509 (2014).
(31) X. Yu, H. J. Kim, J.-Y. Hong, Y. M. Jung, K. D. Kwon, J. Kong, and H. S. Park, *Nano Energy*, **15**, 576 (2015).
(32) L.-F. Chen, Z.-H. Huang, H.-W. Liang, H.-L. Gao, and S.-H. Yu, *Adv. Funct. Mater.*, **24**, 5104 (2014).
(33) Z.-S. Wu, A. Winter, L. Chen, Y. Sun, A. Turchanin, X. Feng, and K. Müllen, *Adv. Mater.*, **24**, 5130 (2012).
(34) X. Yu, L. Feng, and H. S. Park, *J. Power Sources*, **390**, 93 (2018).